Comprehensive Analysis and Optimized Control of Torque Ripple and Power Factor in a Three-Phase Mutually Coupled Switched Reluctance Motor With Sinusoidal Current Excitation

Peter Azer, *Member, IEEE*, Berker Bilgin, *Senior Member, IEEE*, and Ali Emadi, *Fellow, IEEE*

***Abstract*—This article presents a comprehensive analysis of torque ripple and power factor for three-phase mutually coupled switched reluctance motors (MCSRMs) with sinusoidal current excitation. MCSRMs controlled by sinusoidal currents have the advantage of using the conventional voltage source inverter and the conventional vector control. However, MCSRMs are characterized by high torque ripple and low power factor. The torque harmonics due to the sinusoidal current excitation are investigated, and the effect of the current excitation angle on the motor saturation level and the power factor is analyzed. These analyses are then used in the development of an optimized control method to reduce torque ripple and to increase power factor and average torque. In the proposed control method, the power factor and phase voltage are calculated by the knowledge of the phase flux linkage and phase current. The phase flux linkage is represented in terms of Fourier coefficients, where these coefficients are functions of direct- and quadrature-axis currents. Hence, they are estimated from 2-D lookup tables (LUTs), which are independent of rotor position. Similarly, the Fourier coefficients of the torque harmonics are also estimated from the 2-D LUTs. The independence of the LUTs from rotor position reduces the size of the LUTs significantly. The proposed control method is validated by experiments on a 2-kW 12/8 MCSRM.**

***Index Terms*—Finite-element method, Fourier series, genetic algorithm, motor control, power factor, reluctance machine, sinusoidal current excitation, torque ripple, vector control.**

I. INTRODUCTION

Switched reluctance motors (SRMs) have a simple, low cost, and robust structure as they do not have rotor magnets or rotor windings [1]. However, SRMs suffer from high torque ripple and acoustic noise [2], and they can have lower efficiency and power density compared to the permanent magnet synchronous motors. The conventional SRMs (CSRMs) are based on single-phase excitation, and torque production is due to the change of self-inductance. The mutual inductance in a CSRM between phases can generally be ignored [1]. CSRMs require an asymmetric bridge converter for each phase to provide unidirectional phase currents, and an independent current control can be achieved by this way [3], [4]. In the CSRM, reduction of the torque ripple and radial forces for the dominant vibration mode shapes is mainly based on current shaping techniques, where a phase current waveform is defined as a function of rotor position for different operating conditions [5]. That approach might require significant memory when the entire operating range is covered in a motor drive with a wide speed range. Hysteresis current control is commonly used for tracking the shape of the current reference. Hysteresis control can also contribute to acoustic noise due to its variable switching frequency [6]. The challenges in CSRMs in terms of using an asymmetric bridge converter and the potential control complexities can be addressed by using a mutually coupled SRM (MCSRM) [7].

MCSRMs are based on multiphase excitation; thus, torque production is a result of the change of self- and mutual inductances. The winding configuration of MCSRMs differs from that of CSRMs to increase the mutual coupling between phases [1]. The windings configuration of an MCSRM can be single-layer short- or full-pitched and double-layer short-pitched [1]. Single- and double-layer short-pitched configurations are both for CSRM and MCSRM. The single-layer full-pitched configuration is only for MCSRM as it requires at least two phases to be excited to magnetize a single stator pole. Several phase current waveforms can be used in MCSRMs, including unipolar rectangular waveform [8]–[10], bipolar rectangular waveform [11]–[13], or sinusoidal current waveform [14]–[17]. The three-phase MCSRM controlled by sinusoidal currents can be considered as an ac machine and the conventional voltage-source inverter (VSI) can be used. Moreover, the standard vector control can be applied, and the regular pulsewidth modulation (PWM) techniques, such as space vector modulation (SVM) and sinusoidal PWM, can be utilized [15], [16]. According to the analysis provided in [15], full-pitched MCSRMs have the highest efficiency compared to other winding configurations when they are controlled with sinusoidal currents. In [15], it was also shown that the full-pitched MCSRM has higher torque

---

Manuscript received April 21, 2020; revised July 18, 2020 and October 5, 2020; accepted November 12, 2020. Date of publication November 17, 2020; date of current version February 5, 2021. This work was supported in part by the Natural Sciences and Engineering Research Council of Canada. Recommended for publication by Associate Editor G. De Donato. *(Corresponding author: Peter Azer.)*

The authors are with the McMaster Institute for Automotive Research and Technology, McMaster University, Hamilton, ON L8S 4K1, Canada (e-mail: eliap@mcmaster.ca; bilginb@mcmaster.ca; emadi@mcmaster.ca).

Color versions of one or more figures in this article are available at https://doi.org/10.1109/TPEL.2020.3038741

Digital Object Identifier 10.1109/TPEL.2020.3038741

density and power factor and lower torque ripple. According to [17], the double-layer short-pitched MCSRMs can provide improved torque density and torque ripple when they are controlled with sinusoidal currents as compared to the case when it is excited with other current waveforms. The existing control methods in the literature for MCSRMs with sinusoidal current excitation are based on maximum torque per ampere control, where direct- and quadrature-axis currents are equal. In those methods, torque ripple and power factor are not considered [14], [18], [19]. Another control method was introduced in [20], where torque ripple is reduced by injecting the third-order current harmonic for the single-layer short- and full-pitched MCSRM. However, the disadvantage of injecting the third-order harmonic is the existence of the zero-sequence component, and hence, an additional leg for the VSI connected to the neutral point is required. Li *et al.* [20] also showed that the torque ripple can be reduced in the double-layer MCSRM by injecting the fifth- and seventh-order current harmonics. However, the torque ripple is reduced on the expense of reducing the average torque by more than 10%.

The control methods proposed in the literature usually focus on one performance parameter. For instance, the authors in [14], [18], and [19] focus only on motor efficiency, while the authors in [20] focus only on minimizing the torque ripple. In this article, the effect of direct- and quadrature-axis currents on torque ripple, saturation level, efficiency, and power factor is first analyzed. Then, an optimized control method is developed to improve the power factor, torque ripple, and average torque. Power factor is calculated from the knowledge of the phase current and phase flux linkage. The phase flux linkage is represented by the sine and cosine Fourier coefficients. These coefficients are estimated from lookup tables (LUTs) as a function of direct- and quadrature-axis currents. Hence, the LUTs have two dimensions, and they are independent of the rotor position. Likewise, the torque harmonics are also represented as Fourier coefficients in 2-D LUTs.

The rest of this article is organized as follows. Section II analyzes the sources of torque ripple in MCSRMs with sinusoidal current excitation. Section III analyzes the effect of the current excitation angle and saturation level on power factor. Section IV presents the proposed optimized control method for MCSRMs. Section V validates the proposed method with experiments. Finally, Section VI concludes this article.

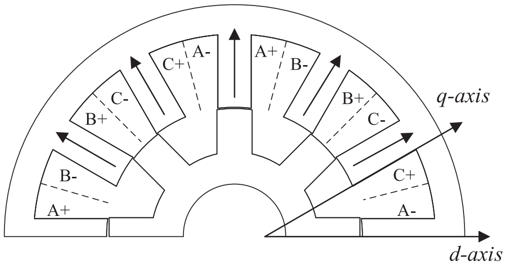

Fig. 1. Winding configuration and flux paths of three-phase 12/8 MCSRM.

TABLE I
SPECIFICATIONS OF MOTOR USED IN INVESTIGATION

Parameter	Value	Parameter	Value
Phase number	3	Rotor outer radius	41.5 mm
Stator poles	12	Rotor inner radius	30.5 mm
Rotor poles	8	Shaft radius	12.5 mm
Axial length	70 mm	Turns per phase	28
Stator outer radius	68 mm	peak current	21.21A
Stator inner radius	56.7 mm	Rated torque	3Nm

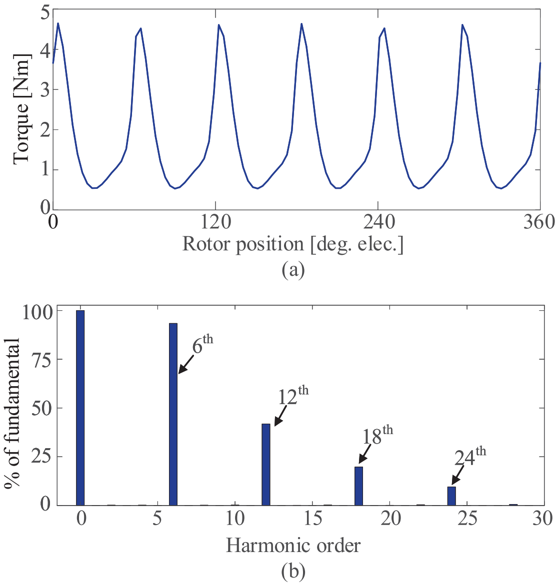

(a)

(b)

Fig. 2. (a) Generated torque waveform from the FEA model when $[i_d, i_q] =$ [4,20] A and (b) its harmonic content.

II. TORQUE RIPPLE ANALYSIS

In order to conduct torque ripple and power factor analysis, a three-phase 12/8 SRM has been used in this article. The motor used in this investigation is designed to operate as a CSRM. The winding configuration has been changed to operate it as an MCSRM. Fig. 1 shows the winding configuration and the flux directions for the three-phase 12/8 MCSRM. The motor specifications are shown in Table I. Finite-element analysis (FEA) has been conducted to analyze the torque ripple behavior of this motor with sinusoidal current excitation. The harmonic content of the generated torque waveform is shown in Fig. 2 when the d-axis current (i_d) and q-axis current (i_q) are equal to 4 and 20 A, respectively. It can be noticed from Fig. 2(b) that the generated torque waveform has a dc component in addition to the 6th-, 12th-, 18th-, and 24th-order harmonics. Therefore, it can be expressed in Fourier series as

$$\begin{aligned} T_e(t) = T_{\text{avg}} &+ T_{6a}\sin(6wt) + T_{6b}\cos(6wt) \\ &+ T_{12a}\sin(12wt) + T_{12b}\cos(12wt) \\ &+ T_{18a}\sin(18wt) + T_{18b}\cos(18wt) \\ &+ T_{24a}\sin(24wt) + T_{24b}\cos(24wt) \end{aligned} \tag{1}$$

where w is the angular frequency, T_{avg} is the dc component and, hence, the average torque. T_{6a} is the Fourier sine coefficient of

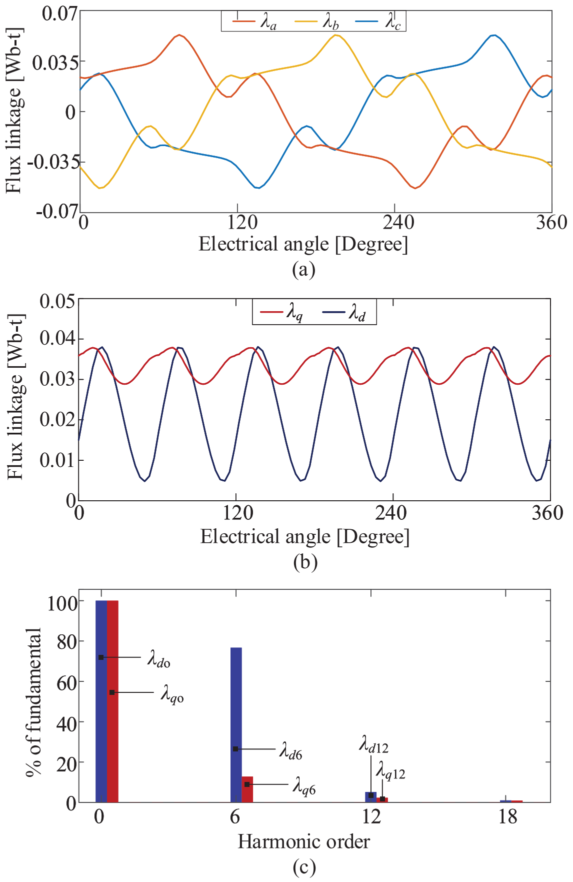

(a)

(b)

(c)

Fig. 3. (a) Three-phase flux linkage at $[i_d, i_q] = [4, 20]$ A. (b) Direct- and quadrature-axis flux linkages and their (c) harmonic content at $[i_d, i_q] = [4, 20]$ A.

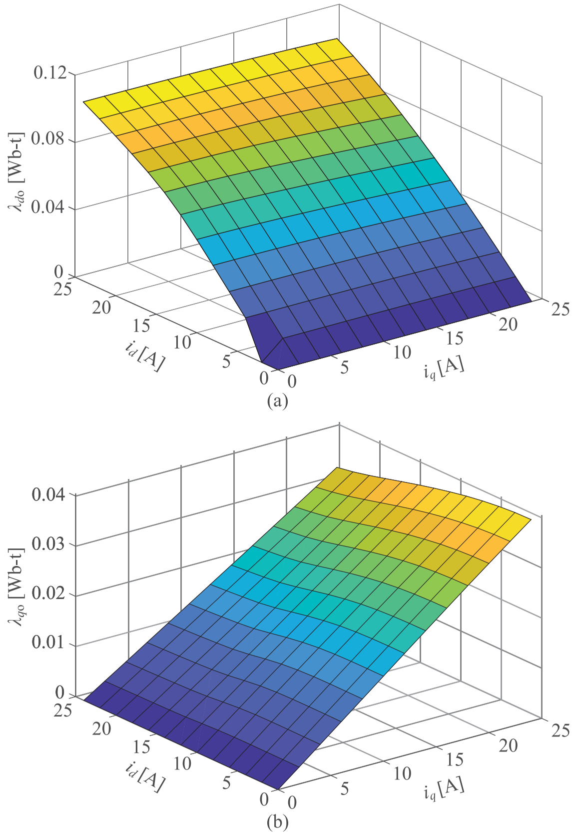

(a)

(b)

Fig. 4. Nonlinear relationship of (a) λ_{do} and (b) λ_{qo} with respect to direct- and quadrature-axis currents.

the sixth-order harmonic, and likewise for T_{12a}, T_{18a}, and T_{24a}. T_{6b} is the Fourier cosine coefficient of the sixth-order harmonic, and likewise for T_{12b}, T_{18b}, and T_{24b}. The average torque T_{avg} is calculated as [21]

$$T_{\text{avg}} = \frac{3}{2} p(\lambda_{do} i_q - \lambda_{qo} i_d) \tag{2}$$

where λ_{do} and λ_{qo} represent the fundamental direct- and quadrature-axis flux linkages, respectively, which are the dc values when the three-phase flux linkages are transformed into the dq frame. Fig. 3(a) shows the three-phase flux linkages from the FEA model for $[i_d, i_q] = $ [4,20] A. The corresponding direct- and quadrature-axis flux linkages and their harmonic content are shown in Fig. 3(b) and (c), respectively. From Fig. 3(c), the direct- and quadrature-axis flux linkages can also be expanded by Fourier series

$$\begin{aligned} \lambda_d(t) = \lambda_{do} \lambda_{d6} \sin(6wt + \alpha_6) \\ + \lambda_{d12} \sin(12wt + \alpha_{12}) \end{aligned} \tag{3}$$

$$\begin{aligned} \lambda_q(t) = \lambda_{qo} + \lambda_{q6} \cos(6wt + \beta_6) \\ + \lambda_{q12} \cos(12wt + \beta_{12}) \end{aligned} \tag{4}$$

where λ_{d6} and λ_{d12} are the 6th- and 12th-order harmonics of the d-axis flux linkage, respectively, and α_6 and α_{12} are their respective phase angles. λ_{q6} and λ_{q12} are the 6th- and 12th-order harmonics of the q-axis flux linkage, and β_6 and β_{12} are their respective phase angles. The 6th and 12th orders are due to spatial harmonics. In order to calculate the average torque from (2), the zero-order Fourier coefficients of the direct- and quadrature-axis flux linkage λ_{do} and λ_{qo} are estimated from 2-D LUTs as

$$\lambda_{do} = f_d(i_d, i_q) \tag{5a}$$

$$\lambda_{qo} = f_q(i_d, i_q) \tag{5b}$$

where $f_d(i_d, i_q)$ and $f_q(i_d, i_q)$ are 2-D LUTs independent of the rotor position, since they represent the Fourier coefficients in (3) and (4) and not the instantaneous values. These LUTs describe the nonlinear relationship between λ_{do} and λ_{qo} with respect to i_d and i_q. Fig. 4 shows the 2-D LUTs $f_d(i_d, i_q)$ and $f_q(i_d, i_q)$.

It can also be observed from the torque waveform in Fig. 2 that the sixth-order harmonic has the largest magnitude among all other present harmonics. These harmonics generate the torque ripple. Therefore, by minimizing the sixth-order harmonic, we achieve significant reduction in torque ripple. The Fourier coefficients of the sixth-order harmonic T_{6a} and T_{6b} are represented as follows:

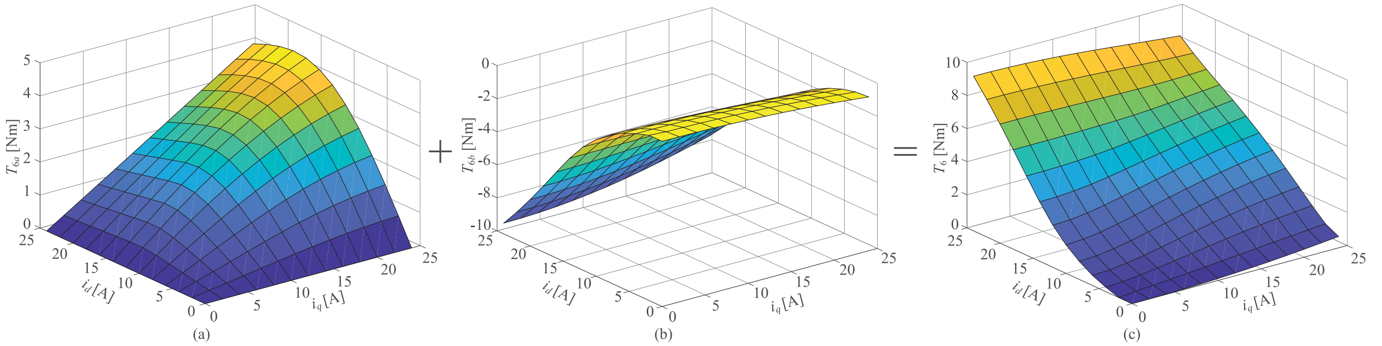

Fig. 5. Fourier coefficients of the sixth-order torque harmonic (a) T_{6a} and (b) T_{6b}, and (c) vector summation of T_{6a} and T_{6b}.

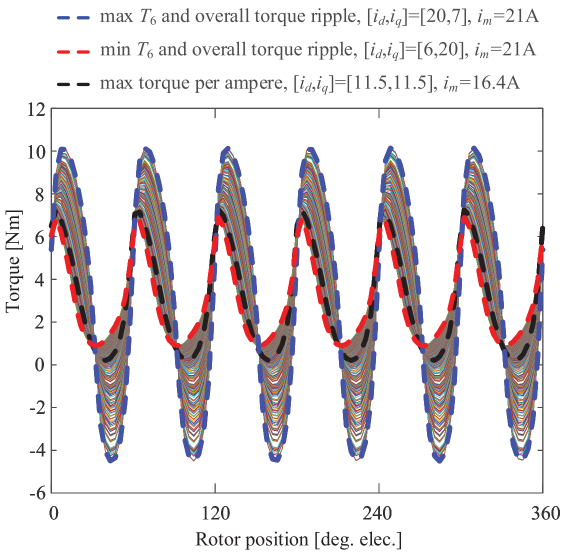

Fig. 6. Torque waveforms from the FEA model at 3-N · m average torque.

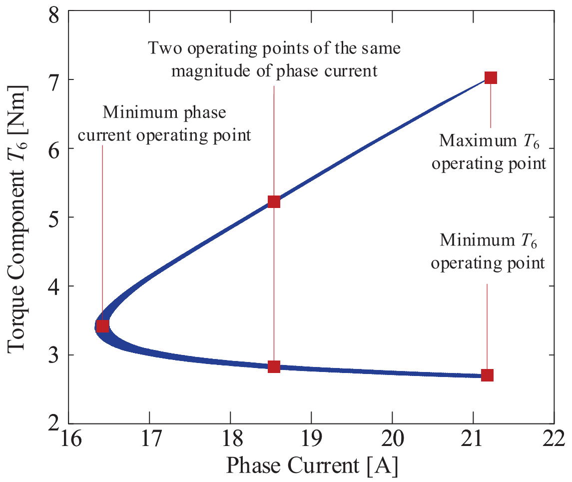

Fig. 7. Nonlinear relationship of torque ripple (T_6) with respect to phase current magnitude.

$$T_{6a} = f_{6a}(i_d, i_q) \tag{6a}$$

$$T_{6b} = f_{6b}(i_d, i_q) \tag{6b}$$

where $f_{6a}(i_d, i_q)$ and $f_{6b}(i_d, i_q)$ are 2-D LUTs, and they describe the nonlinear relationship between T_{6a} and T_{6b} with respect to i_d and i_q. Hence, the magnitude of sixth-order harmonic T_6 is calculated as

$$T_6 = \sqrt{T_{6a}^2 + T_{6b}^2}. \tag{7}$$

Fig. 5 shows the 2-D LUTs, $f_{6a}(i_d, i_q)$ and $f_{6b}(i_d, i_q)$, and their vector summation based on (7). There is an infinite number of $[i_d, i_q]$ operating points that can achieve a certain average torque. These operating points have different phase current magnitude, torque ripple, and power factor. As an example, for an average torque T_{avg} of 3 N · m, the range of direct- and quadrature-axis currents is swept and the operating points are found using (2) and (5). Then, these operating points are simulated using the FEA model. Fig. 6 shows the torque waveforms from the FEA model that achieve T_{avg} of 3 N · m. It can be noticed from Fig. 6 that these operating points achieve the same average torque but with different torque ripples.

Fig. 7 describes the behavior of the torque ripple for the operating points in Fig. 6. The torque ripple is represented by the magnitude of T_6 with respect to the phase current magnitude, by the help of (6). It can be noticed that the operating point corresponding to the minimum torque ripple has the largest phase current magnitude and, hence, the highest copper loss. In contrast, the operating point that corresponds to the minimum phase current magnitude has a relatively higher torque ripple. As it will be shown in the next section, this operating point also has a low power factor. Therefore, from the controls perspective, if the phase currents are optimized to achieve the lowest torque ripple, that would result in the highest copper loss. If only the magnitude of phase current is optimized, that would result in a low power factor and a relatively higher torque ripple. It should be noted that the waveform in Fig. 7 is a quadratic function with respect to the torque ripple component, T_6. Therefore, there are two operating points with the same phase current magnitude and same average torque T_{avg} of 3 N · m, but with different T_6. The implications of this behavior will be discussed in more detail in the next section.

Note that the waveforms in Figs. 6 and 7 are the same for any speed, as the average torque was calculated from (2) and the sixth-order torque harmonic was calculated from (6). Both expressions are dependent on d- and q-axis currents, but they are independent of the motor speed. The implication of speed will also be discussed in the next section. The higher the speed, the higher the induced voltage, which, in turn, requires higher phase voltage to inject the same phase current.

Before finishing this section, the authors would like to address why the analyzed motor has high torque ripples, as shown in Figs. 6 and 7. As mentioned earlier, the motor used in this investigation is designed to operate as a CSRM with single-phase unipolar current excitation and not as MCSRM with multiphase sinusoidal current excitation. Motors those are specifically designed to operate as an MCSRM with sinusoidal current excitation have been reported to have approximately five times lower torque ripple compared to the motor used in this investigation [14], [18]–[20].

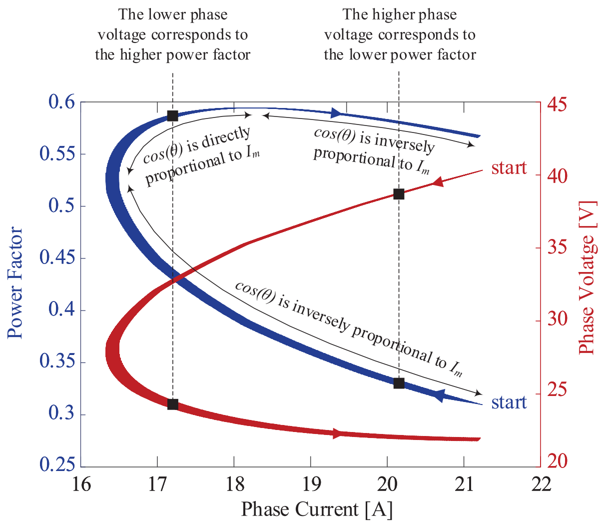

Fig. 8. Nonlinear relationship of phase voltage and power factor with respect to phase current magnitude.

III. Power Factor Analysis

Power factor affects the performance of both the motor and the inverter. From the inverter side, higher power factor means that less reactive power is supplied for the same apparent power. Thus, the size and the rms current of the dc-link capacitor can be reduced. The higher power factor also reduces the volt–ampere rating of the converter. From the motor perspective, power factor influences the core losses [22], and it reflects the saturation level of the motor [23]. In a saturated-magnetic system, the area corresponding to the co-energy on the flux linkage–current characteristics is larger than the area corresponding to the field energy. The co-energy represents the energy converted into mechanical energy. The field energy represents the magnetic energy stored in the system. Therefore, in an SRM, the ratio between the co-energy and field energy is equivalent to the ratio between the real power and reactive power, and it represents the power factor. Hence, a higher power factor can be achieved in an SRM when it operates at a higher saturation level. Due to its excitation principles and winding configuration, the majority of the flux in CSRM is in the radial direction [24]. This helps with the core saturation, but also results in stronger radial forces that would excite the stator core. The excitation principles in the MCSRM results in lower radial flux, which, in turn, results in smaller radial forces [16], [25]. However, this also results in less effective core saturation as compared to the CSRM. In other words, the MCSRM saturates at higher current levels as compared to the CSRM. This is the major factor for why the power factor of the MCSRM is relatively low as compared to the CSRM.

Power factor can be calculated for the operating points that achieve 3-N · m average torque in Fig. 6. The fundamental direct- and quadrature-axis voltages v_d and v_q are first calculated at given direct- and quadrature-axis currents and given speed [21]

$$v_d = i_d R - \lambda_{qo} w \tag{8a}$$

$$v_q = i_q R + \lambda_{do} w \tag{8b}$$

where R is the phase winding resistance and λ_{do} and λ_{qo} are found from (5). After calculating the fundamental voltage components, the power factor can be calculated based on the real power P and the reactive power Q [21]

$$P = \frac{3}{2}(v_d i_d + v_q i_q) \tag{9a}$$

$$Q = \frac{3}{2}(v_q i_d - v_d i_q) \tag{9b}$$

$$\cos(\phi) = \frac{P}{\sqrt{P^2 + Q^2}} \tag{9c}$$

where $\cos(\phi)$ is the power factor. Fig. 8 shows the power factor and phase voltage with respect to the phase current magnitude for the operating range that achieves 3-N · m average torque at 1000 r/min. It can be noticed from Fig. 8 that the same magnitude of phase current can be created by two different voltage magnitudes. For the same phase current magnitude, the operating point that corresponds to a lower phase voltage also corresponds to a higher power factor. This can be observed in Fig. 8 by following the direction of the power factor and phase voltage curves designated by the arrows. The operating point with the higher power factor has lower induced electromotive force (EMF), so that the same magnitude of phase current is generated with a lower phase voltage. This can simply be quantified by expressing the phase voltage for single-phase excitation [24]

$$v_a = i_a R + \underbrace{\left(L_a(\theta) \frac{di_a}{dt} + i_a \frac{dL_a(\theta)}{d\theta} w \right)}_{\text{induced EMF}} \tag{10}$$

where v_a is the phase voltage, i_a is the phase current, and L_a is the phase inductance. Equation (10) shows that the phase voltage depends on the phase current, phase resistance, phase inductance, and motor speed w. For the same motor speed, phase current, and phase resistance, v_a depends on the phase inductance, L_a. As the core saturates, the magnitude of L_a

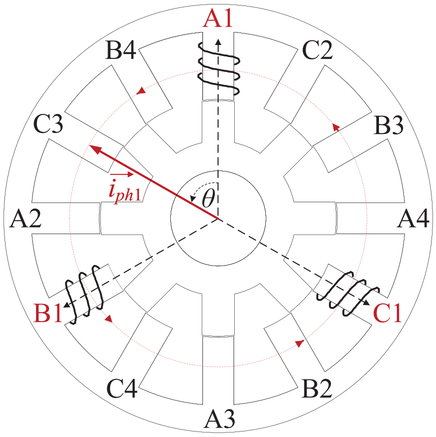

Fig. 9. Rotating current vector i_{ph1} due to three phases shifted in time and space by 120°.

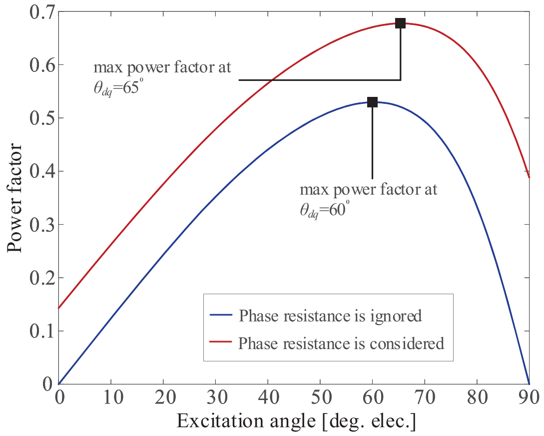

Fig. 10. Power factor with respect to the current excitation angle at $I_m = 18$ A with and without considering the phase resistance.

decreases, which, in turn, limits the induced EMF. This enables injecting the same magnitude of current with a lower phase voltage.

In Fig. 8, the blue curve describing the relationship between the power factor and phase current can be divided into three regions. In the majority portion of the curve, the power factor is inversely proportional to the magnitude of the phase current. This implies that the saturation level represented by the power factor does not necessarily increase with the phase current magnitude. The location of the current vector has a significant effect on the power factor, as well. The current phasor is a rotating vector in space, and its magnitude I_m is defined by the direct- and quadrature-axis components

$$I_m = \sqrt{i_d^2 + i_q^2}. \tag{11}$$

In a balanced three-phase ac machine, the phase windings are distributed 120° apart in space, and the electrical phase shift between phases is 120°. This creates a current vector, i_{ph1}, that has a constant magnitude of I_m, and it rotates uniformly in space (see Fig. 9). The instantaneous position of the current phasor depends on the vector summation of the instantaneous values of the three-phase currents. The 12/8 SRM has four coils per phase, and hence, there are four sets of 120° phase-shifted abc coils, and the phase shift between each set is 90° (see Fig. 9). Therefore, there are four current phasors in space, and they are 90° phase shifted from each other. For the coil set shown in Fig. 9, the current phasor can be expressed as

$$\vec{i}_{ph1} = \underbrace{i_a(t) + i_b(t)}_{\text{instantaneous values}} \underbrace{e^{j\frac{-2\pi}{3}}}_{\text{position in space}} + i_c(t)e^{j\frac{2\pi}{3}} \tag{12a}$$

$$= I_m e^{j\theta}, \quad \theta = 0 \to 2\pi \tag{12b}$$

where $i_a(t)$, $i_b(t)$, and $i_c(t)$ are the instantaneous values of the phase currents, and θ is the instantaneous position of the current phasor in space. The initial position, when $t = 0$, of the current phasor, i_{ph1}, is defined by the current excitation angle θ_{dq}

$$\theta_{dq} = \tan^{-1}\left(\frac{i_q}{i_d}\right) \tag{13a}$$

$$\theta = \theta_{dq} + wt, \quad wt = 0 \to 2\pi. \tag{13b}$$

The initial position ($\theta = \theta_{dq}$) is when the rotor is aligned with the stator poles of phase a, as shown in Fig. 9. At that position and for counterclockwise direction of rotation, magnetizing the stator poles of phase c will generate positive torque. In other words, the current phasor should be aligned with the stator poles of phase c, where the initial angle θ_{dq} would be 60°. The closer the current phasor to the stator poles of phase c, a higher saturation level it will achieve, and hence, the higher the power factor will be. For instance, the two operating points from the operating range that achieves 3-N · m average torque $[i_d, i_q] = [8.4, 16]$ A and $[i_d, i_q] = [15.9, 8.6]$ A have the same current magnitude of 18 A, but their power factor at 1000 r/min is 0.67 and 0.46, respectively. The first operating point has a higher power factor as its current phasor is closer to the stator poles of phase c at the initial position, $\theta_{dq} = 62°$, compared to the second point, which has an excitation angle of $\theta_{dq} = 28°$. In order to confirm that the maximum power factor is achieved at $\theta_{dq} = 60°$, Fig. 10 shows two conditions for the power factor with respect to the excitation angle when $I_m = 18$ A. The first condition is when the phase resistance R is ignored, and it reveals that the maximum power factor happens at $\theta_{dq} = 60°$. At this excitation angle, the current phasor is aligned with phase c, which at the given rotor position generates torque in the counterclockwise rotation and achieves the highest saturation level. In the second condition in Fig. 10, the phase resistance is not ignored. Then, the total real power P equals the sum of the real power consumed by the motor and the power loss due to the phase resistance, ${I_m}^2R$. As a result, the maximum power factor occurs at $\theta_{dq} = 65°$ as it depends not only on the motor saturation level, but also on ${I_m}^2R$ losses. In the rest of this article, the phase resistance R is taken into account when calculating the power factor.

Fig. 11 shows the relationship between the power factor and the current excitation angle θ_{dq} for the operating range that

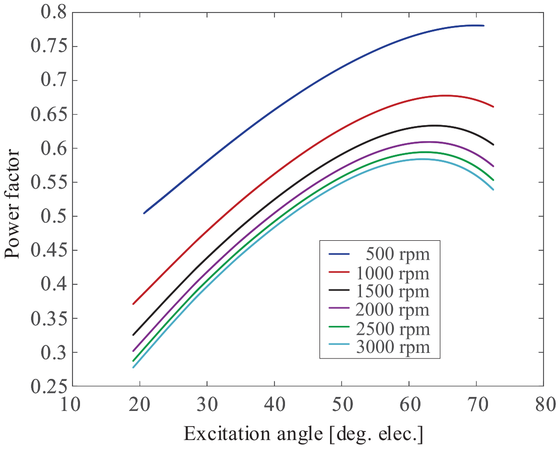

Fig. 11. Nonlinear relationship of power factor with respect to current excitation angle θ_{dq} at different speeds for 3-N · m average torque.

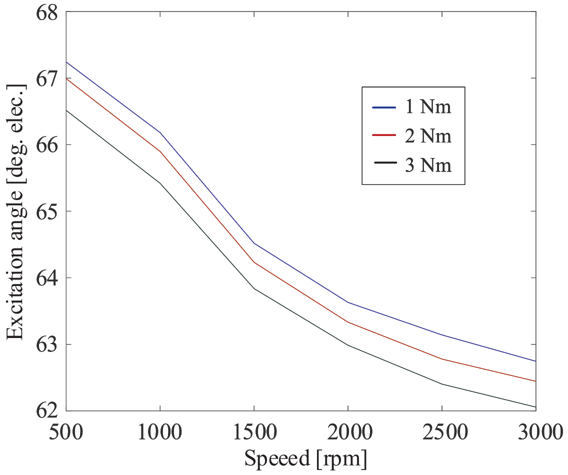

Fig. 12. Nonlinear relationship of current excitation angle θ_{dq} corresponding to the maximum power factor with respect to speed at different torque conditions.

achieves the 3-N · m average torque at different speeds. Fig. 11 reveals that the power factor increases until it reaches a certain excitation angle, and then, it starts to decrease. Fig. 12 shows the excitation angles corresponding to the maximum power factor at different speeds for average torque of 1, 2, and 3 N · m. It can be seen that the maximum power factor always happens at an excitation angle between 62° and 67°. As mentioned before, the maximum power factor is not at $\theta_{dq} = 60^\circ$ due to the ${I_m}^2R$ losses and the different current magnitude I_m for the operating range that achieves the same average torque.

In order to show how the location of the current phasor affects the magnetization of stator poles, Fig. 13 shows the magnetic flux path at the aligned position for the maximum and minimum power factor operating points achieving $T_{\mathrm{avg}} = 3\,\mathrm{N}\cdot\mathrm{m}$ at 1000 r/min. It can be observed that when the current excitation angle is 65°, the current phasor is approximately aligned with the stator poles of phase c. In other words, the 65° current phasor is magnetizing the unaligned stator poles of phase c, which are responsible for torque production. When the excitation angle is 19°, the current phasor is closer to phase a. However, the rotor poles are already aligned with phase a; therefore, this excitation angle generates the minimum torque, since there is no variation in reluctance. When the rotor aligns with phase c after 15 degrees of rotation, the current vector rotates 60° in the same direction, as the electrical frequency is four times the mechanical frequency. The 60° rotation of the current phasor makes it aligned with phase b to magnetize its stator poles similar to what happened with the stator poles of phase c at the initial rotor position.

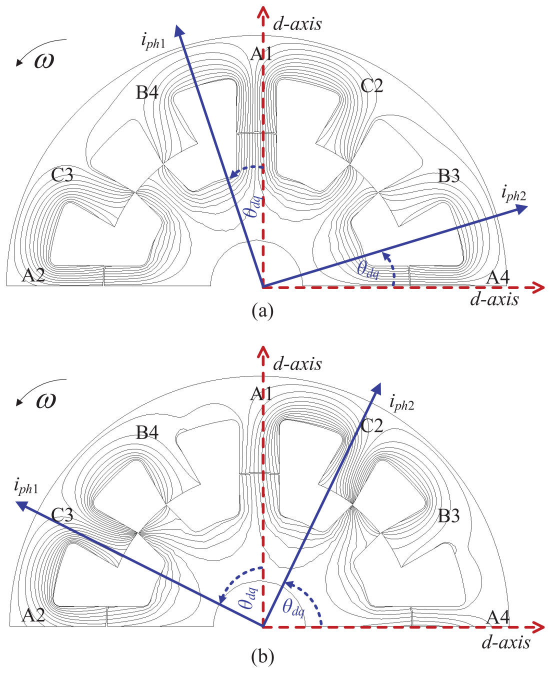

Fig. 13. Current phasors at the initial rotor position ($\theta = \theta_{dq}$) and 1000 r/min. (a) Minimum power factor operating point $\vec{i}_{\mathrm{ph1}} = 21.1\angle\, 19^\circ$. (b) Maximum power factor operating point $\vec{i}_{\mathrm{ph1}} = 18.9\angle\, 65^\circ$.

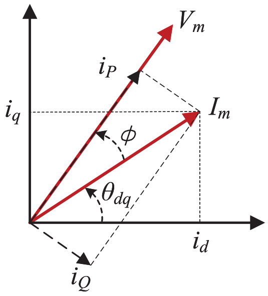

Fig. 14. Currents components responsible for real and reactive powers i_P and i_Q.

In order to explicit the difference between the maximum power factor and the maximum torque per ampere operating points, the phase current is decoupled into two components i_P and i_Q, as shown in Fig. 14. i_P is the current component responsible for the real power as it is in phase with the voltage vector V_m. i_Q is the current component responsible for the reactive power

$$i_P = I_m \cos(\phi) \tag{14a}$$

$$i_Q = I_m \sin(\phi) \tag{14b}$$

$$I_m = \sqrt{i_P^2 + i_Q^2}. \tag{14c}$$

The real power P and reactive power Q can be reformulated using (14) as

$$P = 3\frac{V_m}{\sqrt{2}}\frac{I_m}{\sqrt{2}}\cos(\phi) = 3\frac{V_m}{2}i_P \tag{15a}$$

$$Q = 3\frac{V_m}{\sqrt{2}}\frac{I_m}{\sqrt{2}}\sin(\phi) = 3\frac{V_m}{2}i_Q \tag{15b}$$

$$\cos(\phi) = \frac{P}{\sqrt{P^2 + Q^2}} = \frac{i_P}{I_m}. \tag{15c}$$

From (15c), it is clear that the power factor is dependent on both i_P and I_m. Thus, the maximum power factor maximizes the ratio i_P/I_m regardless of how much I_m is. The maximum torque per ampere operating point minimizes the total current I_m regardless of how much is i_P or i_Q.

IV. OPTIMIZED PERFORMANCE FOR MCSRM

Up to this point, we have analyzed the torque ripple and power factor in the MCSRM for sinusoidal current excitation. In this section, the selection of the optimized direct- and quadrature-axis currents will be discussed to minimize the torque ripple and maximize the power factor and average torque. The power factor is considered in the optimization process to maximize the dc-link utilization. As shown in Section III, for the same magnitude of phase current at the same speed, the required phase voltage has lower magnitude when the power factor is higher (see Fig. 8). Thus, optimizing the power factor maximizes the dc-link utilization to cover wider speed range. For these three performance parameters, the objective function j is formulated as

$$j = \alpha(I_m/I_{\text{rated}}) + \beta(T_6/T_{6\text{rated}}) - \gamma\cos(\phi) \tag{16}$$

$$\alpha + \beta + \gamma = 1 \tag{17}$$

where I_{rated} is the rated current and $T_{6\text{rated}}$ is the maximum T_6, which is 9.5 N · m for the motor used in investigation, as shown in Fig. 5(c). α, β, and γ are the weighting coefficients of the phase current, torque ripple, and power factor, respectively. The available voltage, the rated motor current, and the reference torque constitute the constraints of the optimization problem. The phase current should be less than or equal to the rated motor current considering the thermal limitations, and that is the first constraint. The phase voltage depends on the motor speed, as shown in (8). The optimized operating point is applicable as long as the peak value of line voltage is less than the dc-link voltage. This is the maximum line voltage at unity modulation index when using SVM.

The phase voltage usually includes harmonic components besides the fundamental to remove the spatial harmonics in the phase current and, hence, achieve sinusoidal current excitation. In ac machines, the spatial harmonics due to the slotting effect are usually neglected. However, slotting effect cannot be neglected in SRMs because of high saliency of stator and rotor poles. Those spatial harmonics in the phase current can be removed effectively by harmonic compensation methods, such as proportional–resonant controllers [26]. In this article, we used a feedforward loop to remove the spatial harmonics of the phase current. The feedforward loop injects the corresponding voltage harmonics to ensure sinusoidal current excitation [27]. This ensures that the required phase voltage (fundamental components plus the other harmonics) can be applied at any speed. The peak value of the fundamental phase voltage component should be less than or equal to $(100 - x)\%$ of $v_{\text{dc}}/\sqrt{3}$, where x is the voltage harmonic coefficient, and it defines the room that is kept for the phase voltage harmonics injection. For example, at 500 r/min, the fundamental phase voltage component should be less than or equal to 80% of $v_{\text{dc}}/\sqrt{3}$. Thus, there is a room of 20% for the voltage harmonics injection. The 20% is estimated based on the motor characteristics, and it increases linearly with speed [27]. Notably, the 20% is a high percentage for voltage harmonics at such speed, but this is because the SRM we are using is not designed to operate as an MCSRM with multiphase sinusoidal current excitation [14]. Finally, the average torque must be equal to the reference torque T_{ref}. Hence, the three constraints of the optimization problem can be formulated as

$$\sqrt{i_d^2 + i_q^2} \le i_{\text{rated}} \tag{18a}$$

$$\sqrt{v_d^2 + v_q^2} \le (1 - x)\left(v_{\text{dc}}/\sqrt{3}\right) \tag{18b}$$

$$T_{\text{avg}} = T_{\text{ref}} \tag{18c}$$

where the voltage harmonic coefficient, x, is defined as a function of speed, N_{rpm}, as

$$x = 0.2^{\sim}\frac{N_{\text{rpm}}}{500}. \tag{19}$$

The objective function in (16) combines the three objectives in one function by using the weighting coefficients in (17). In order to identify how to select the weighting coefficients, some analysis has been applied. Fig. 15 shows the optimized operating points at 3 N · m and different speeds when only one weighting coefficient is considered and the other coefficients are set to zero.

As given in (2), the average torque depends on the d- and q-axis currents only, and it is independent of the motor speed. Thus, in Region ① in Fig. 15, the minimum phase current to achieve the reference torque is the same at 500 r/min (×), 1000 rpm (×), 1500 rpm (×), and 2000 rpm (×), but with different power factors. The higher the speed, the higher the induced voltage, which, in turn, requires higher phase voltage to inject the same phase current and results in a lower power factor. T_6 also depends on direct- and quadrature-axis currents, and it is independent of motor speed, as shown in (6). Therefore, the operating points in Region ① have the same T_6 (○). It can be noticed from the results in Region ① that minimizing the phase current results in the highest T_6. It also results in the lowest power factor. For example, the power factor at 2000 r/min in Region ① is lower than the

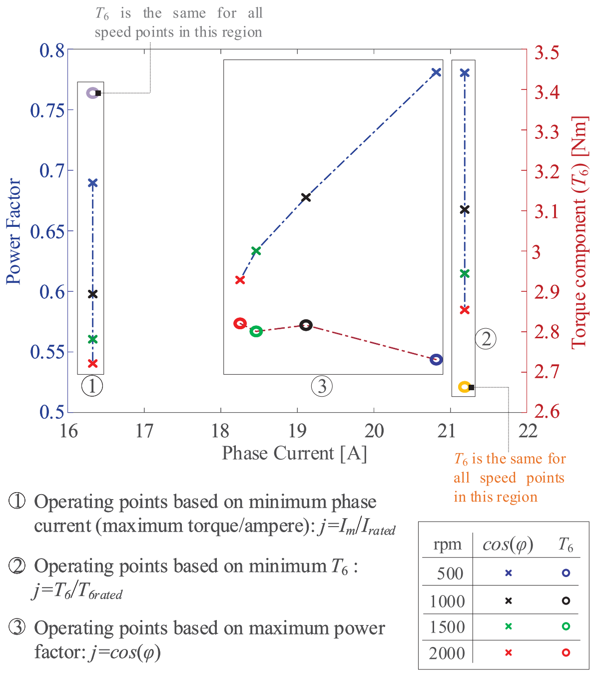

① Operating points based on minimum phase current (maximum torque/ampere): $j=I_m/I_{rated}$

② Operating points based on minimum T_6 : $j=T_6/T_{6rated}$

③ Operating points based on maximum power factor: $j=cos(\varphi)$

rpm	$cos(\varphi)$	T_6
500	×	○
1000	×	○
1500	×	○
2000	×	○

Fig. 15. Optimized operating points at 3 N · m based on the maximum torque per ampere ($j = I_m/I_{\text{rated}}$) are shown in Region ①, the minimum torque ripple ($j = T_6/T_{6\text{rated}}$) are shown in Region ②, and the maximum power factor ($j = \cos(\phi)$) are shown in Region ③.

power factor in Regions ② and ③ for the same operating point. This can be observed by comparing the (×) symbols in the three regions. Region ② in Fig. 15 defines the optimized operating points that have the minimum T_6. Since the operating points in Region ② achieve the same reference torque, they have the same phase current and the same T_6, which is 2.6 N · m (denoted by ○). It can be observed from Fig. 15 that minimizing the torque ripple results in the highest phase current magnitude, which is the motor rated current. For instance, the × symbols in Region ② have higher phase current compared to the × symbols of the same color in Regions ① and ②.

Region ③ defines the operating points, which have the maximum power factor. These operating points have different direct- and quadrature-axis currents, and hence, different T_6 and power factor. T_6 in Region ③ (denoted by ○ symbols in different colors) varies between 2.7 and 2.9 N · m. When the operating points were optimized for the minimum T_6 in Region ②, the minimum value was 2.6 N · m. Therefore, achieving the maximum power factor results in an acceptable T_6, which is close to the minimum value. Additionally, the operating points in Region ③ also have an intermediate magnitude of phase currents between that for Regions ① and ②. Thus, based on the results in Fig. 15, the weighting coefficient of the torque ripple β in (16) can be set to zero, as optimizing the power factor will result in an acceptable T_6. Then, (17) reduces to

$$\alpha + \gamma = 1. \tag{20}$$

In order to define the values of α and γ, the optimization problem has been developed in MATLAB using genetic algorithm. The weighting coefficient α is varied between 0 and 1. The optimization is conducted at different speeds for the rated torque, $T_{\text{avg}} = 3\,\text{N} \cdot \text{m}$. The results are presented in Fig. 16.

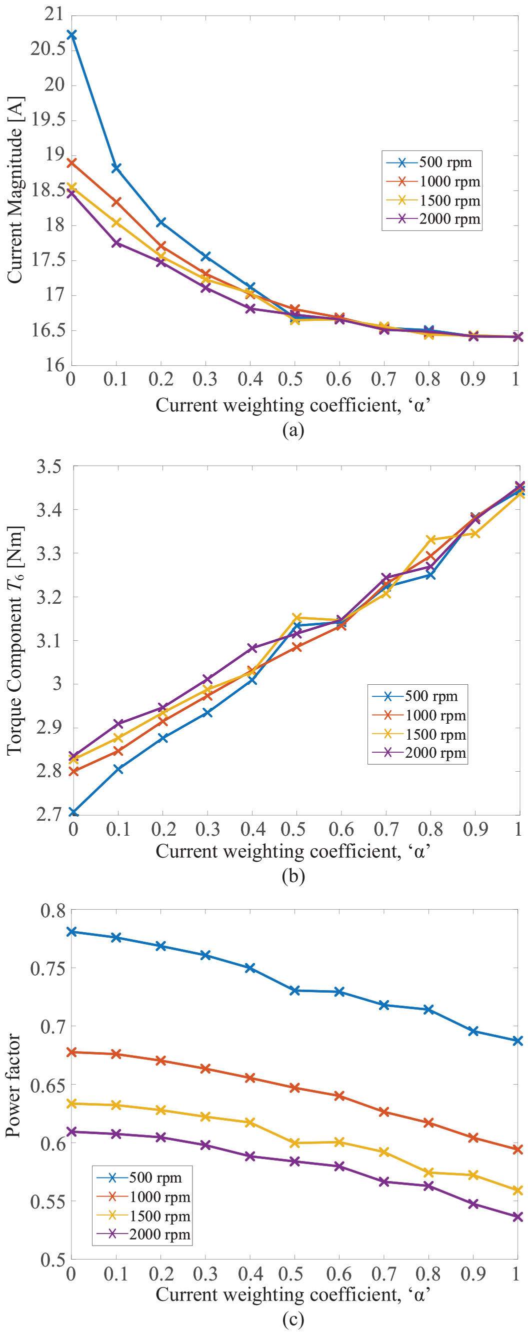

(a)

(b)

(c)

Fig. 16. Variation of (a) phase current magnitude, (b) torque component T_6, and (c) power factor with the current weighting coefficient α for $T_{\text{avg}} = 3\text{N} \cdot \text{m}$.

It can be concluded from Fig. 16(a) that as α increases, the phase current magnitude decreases. This is intuitive, because higher values of α penalize the phase current, as formulated in (20). The weighting coefficient of the power factor γ decreases with the increase of α, since their summation is unity (20). Hence, the power factor reduces with increasing α, as shown in Fig. 16(c). When α exceeds 0.4, the phase current magnitude stays almost constant, but only the power factor reduces. As a result, the current and power factor weighting coefficients α

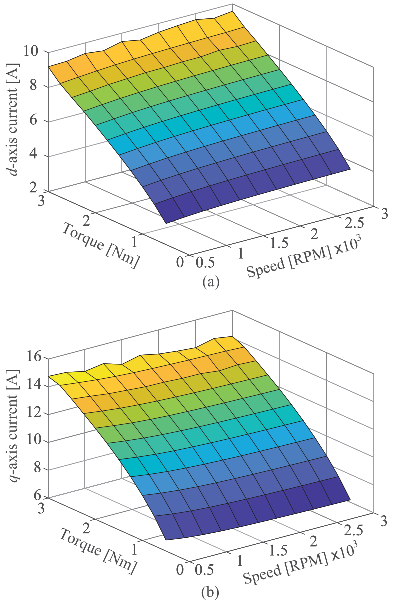

Fig. 17. (a) D-axis current reference and (b) q-axis current reference as a function of torque and speed.

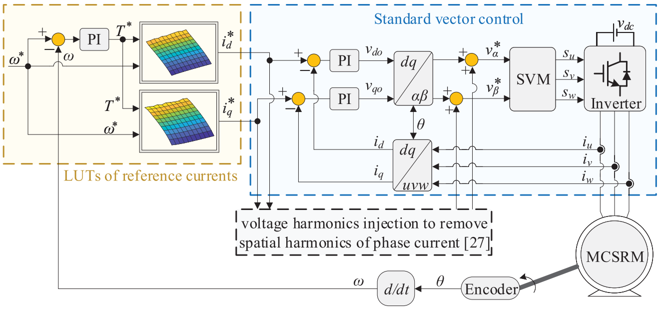

Fig. 18. Integration of LUTs of the reference currents to the standard vector control.

and γ are set to 0.4 and 0.6, respectively. This provides a good agreement among power factor, phase current magnitude, and torque ripple T_6.

The optimized direct- and quadrature-axis currents of the investigated motor for the operating speed and torque ranges are shown in Fig. 17. Fig. 17(a) and (b) shows the LUTs that generate the reference d- and q-axis currents, which achieve the optimum performance at different operating points. These two LUTs are saved in the digital signal processor (DSP). The reference direct- and quadrature-axis currents are then found at the given operating condition by using interpolation function implemented in the DSP. Fig. 18 shows the block diagram of the proposed method. It can be seen that the reference torque is obtained from the speed error. Then, the reference speed and the reference torque are applied to the LUTs in Fig. 17(a) and (b) to obtain the reference direct- and quadrature-axis currents. The reference currents are also applied to the spatial harmonics compensation method in [27] to remove the spatial harmonics of phase current.

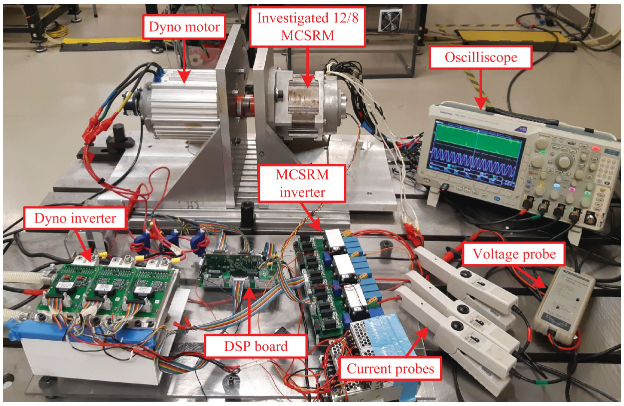

Fig. 19. MCSRM experimental setup.

TABLE II
EXPERIMENTAL SETUP PARAMETERS

Parameter	Value
DC link voltage	200 V
Current sampling frequency	10 kHz
Switching frequency	10 kHz
PI current controller parameters	$k_p = 15,\ k_i = 1000$

V. EXPERIMENTAL RESULTS AND DISCUSSION

For the experimental validation, the MCSRM with the same specifications in Table I is coupled to an interior permanent magnet dyno motor, as shown in Fig. 19. Vector control with SVM is applied to both motor drives. The vector control is implemented in a Texas Instruments TMS320F28377D DSP, and the parameters of the experimental setup are presented in Table II. The instantaneous torque is calculated in the DSP from the torque LUT of the MCSRM by applying the measured phase currents and rotor position as inputs. Then, the calculated torque is converted into an analog signal through a digital-to-analog converter and measured with an oscilloscope by means of a differential probe. The power factor is calculated by postprocessing the recorded phase a voltage and phase a current waveforms in MATLAB.

A. MCSRM Performance at 1000 r/min

First, the performance of the MCSRM was evaluated at 1000 r/min for the rated torque of $T_{\text{avg}} = 3\,\text{N}\cdot\text{m}$. Four operating conditions have been tested: 1) the maximum torque per ampere for $\alpha = 1$; 2) the maximum power factor for $\alpha = 0$; 3) the minimum torque ripple; and 4) the optimized operation for $\alpha = 0.4$. Fig. 20 shows phase a current and the torque waveform for these four operating points. In Fig. 20, the results are presented in a single figure to show the difference between the current and torque waveforms at different operating conditions. Since the test results are obtained separately in individual experiments for each operating point, the phase shift between the current and torque waveforms could not be shown. It can be noticed from Fig. 20 that the phase currents are sinusoidal with negligible distortion. That is due to two reasons: the first reason is that we have used the spatial harmonics compensation method [27],

TABLE III
MCSRM PERFORMANCE AT 1000 r/min

Case	$[i_d, i_q]$(A)	I_m(A)	P(W)	Q(Var)	$cos(\phi)$ Experimental	$cos(\phi)$ Calculated (9)	T_6(Nm)	η(%)
Maximum torque per ampere (α=1)	[11.5, 11.5]	16.4	425	573	0.59	0.59	3.4	74
Maximum power factor (α=0)	[8, 17.1]	18.9	470	510	0.69	0.68	2.7	67
Minimum torque ripple	[7, 20]	21.2	517	575	0.67	0.67	2.6	61
Optimized point (α=0.4)	[8.9, 15.3]	17	441	508	0.65	0.66	2.8	71

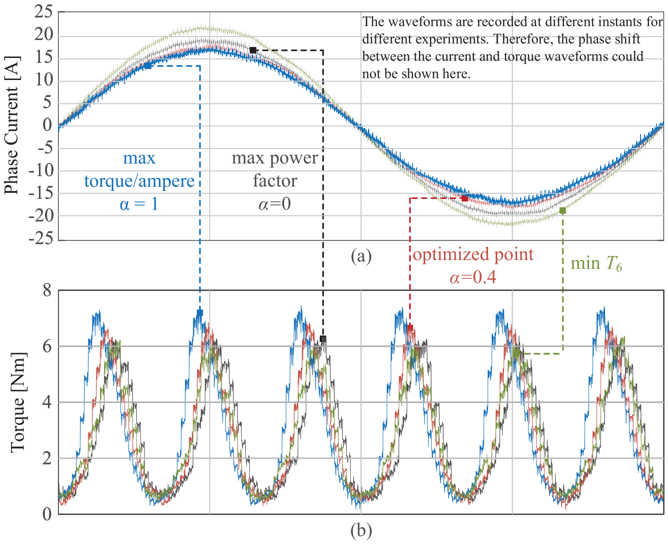

Fig. 20. Experimental results at 1000 and 3 N · m. (a) Phase a current. (b) Electromagnetic torque. Time scale: (4 ms/div).

and the second reason is that the applied line voltage is always within the dc-link limits as constrained in [see 18(b)]. Table III summarizes the motor performance of the operating points presented in Fig. 20. The real power and reactive power are calculated in simulations using (9) after calculating the flux linkage and voltage components from (5) and (8), respectively. In the experiments, the real power and reactive power are calculated using (15), and the power factor is calculated by finding the phase shift between the recorded phase voltage and phase current using Fourier series expansion in MATLAB. The real power, reactive power, and the power factor in simulations and experiments are based on the fundamental components of the phase voltage and current. Real and reactive powers can also exist for other current and voltage harmonics of the same harmonic order. However, since the current harmonics are negligible, the contribution of the harmonics to the power factor could be ignored. It can be noticed from Table III and Fig. 20 that the operating point corresponding to the minimum torque ripple has the minimum T_6 of 2.6 N · m among all the tested operating points. But, it also has the largest magnitude of phase current at 21.2 A, which is the motor rated current. The maximum torque per ampere operating point has the smallest magnitude of phase current, which is 16.4 A. However, it has the highest T_6 of 3.4 N · m and the lowest power factor of 0.59. The operating point corresponding to the maximum power factor has the highest power factor of 0.69 and approximately the same minimum T_6 of 2.7 N · m with a phase current of 18.7 A. The optimized operating point has a power factor of 0.65 with a torque ripple of 2.7 N · m and a phase current of 17 A. Therefore, the optimized operating point provides a combination of high power factor, low torque ripple, and low phase current magnitude. Table III also shows that the power factor calculated from the experimental current and voltage waveforms is in good agreement with the power factor calculated from (9).

It can be observed that the maximum power factor operating point and the optimized operating point draw approximately 11% lower reactive power as compared to the maximum torque per ampere operating point and the minimum torque ripple operating point. The reduction in the reactive power could help reducing the dc-link capacitance.

The motor efficiency η in Table III for each operating point is calculated as

$$\eta = \frac{T_e w_{\text{mech}}}{P}, \quad w_{\text{mech}} = \frac{2\pi N_{\text{rpm}}}{60} \tag{21}$$

where w_{mech} is the mechanical angular frequency, and N_{rpm} is the motor speed in r/min. It can be observed that the motor efficiency is directly proportional to the magnitude of the phase current. Hence, the minimum phase current operating point has the highest efficiency, and the minimum torque ripple operating point has the lowest efficiency, as it has the highest phase current magnitude. Although the efficiency of the optimized point is 3% less than the highest efficiency, it has lower torque ripple and higher power factor. We would like to note that the poor performance of the MCSRM is due to the motor topology, since the motor we are using is not designed to operate as an MCSRM with sinusoidal current excitation.

B. *MCSRM Performance at 1500 r/min*

The performance of the MCSRM is also tested at 1500 r/min. Figs. 21–24 show phase a current and torque waveforms of the maximum torque per ampere operating point, maximum power factor operating point, minimum torque ripple operating point, and the optimized operating point, respectively. Table IV summarizes the experimental results for those four operating points. The higher speed results in higher induced EMF and, hence, lower power factor compared to 1000 r/min.

The operating points corresponding to the maximum torque per ampere and the minimum torque ripple at 1500 r/min draw the same current for the same average torque and deliver the same torque ripple as in the 1000-r/min operation. This is because the average torque and torque ripple are functions of direct- and quadrature-axis currents, and they are independent of the motor speed. Table IV shows that the optimized operating point has lower T_6, lower phase current, and higher power factor. Table IV

TABLE IV
MCSRM PERFORMANCE AT 1500 r/min

Case	$[i_d, i_q]$(A)	I_m(A)	P(W)	Q(Var)	$cos(\phi)$		T_6(Nm)	η(%)
					Experimental	Calculated (9)		
Maximum torque per ampere (α=1)	[11.5, 11.5]	16.4	582	859	0.55	0.56	3.4	81
Maximum power factor (α=0)	[8.2, 16.6]	18.5	624	762	0.63	0.63	2.7	76
Minimum torque ripple	[7, 20]	21.2	675	862	0.62	0.62	2.6	70
Optimized point (α=0.4)	[9, 15.1]	17	598	763	0.61	0.62	2.8	79

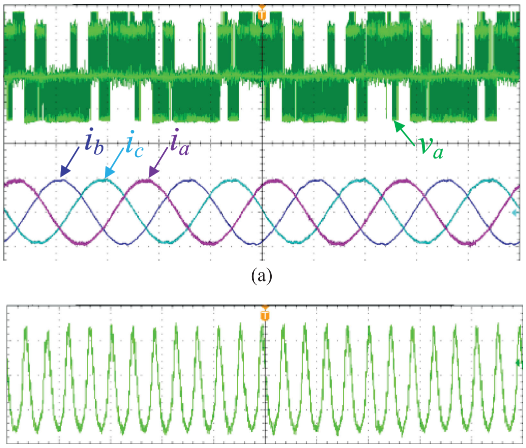

(a)

(b)

Fig. 21. Waveforms corresponding to the maximum torque per ampere at 1500 r/min and 3 N · m. (a) Phase a voltage and the three-phase currents. (b) Electromagnetic torque at 1500 r/min and 3 N · m. Voltage scale: (50 V/div), current scale: (20 A/div), torque scale: (2 N · m/div), and time scale: (4 ms/div).

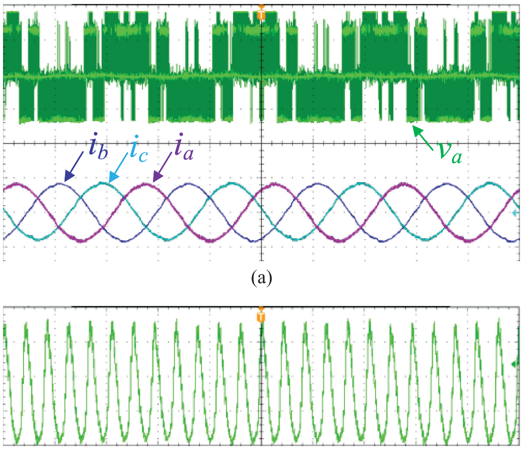

(a)

(b)

Fig. 22. Waveforms corresponding to the maximum power factor at 1500 r/min and 3 N · m. (a) Phase a voltage and the three-phase currents. (b) Electromagnetic torque at 1500 r/min and 3 N · m. Voltage scale: (50 V/div), current scale: (20 A/div), torque scale: (2 N · m/div), and time scale: (4 ms/div).

also shows that the power factor predicted from (9) matches closely with the power factor calculated from the experiments.

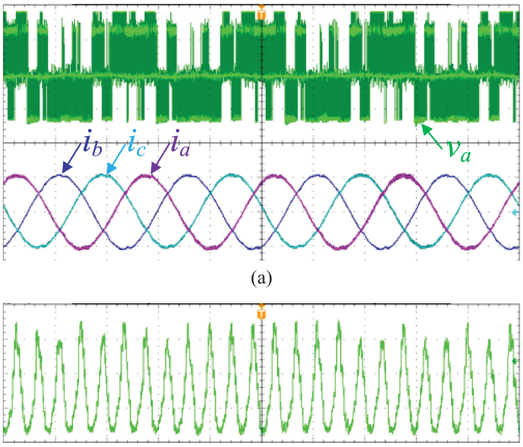

(a)

(b)

Fig. 23. Waveforms corresponding to the minimum torque ripple (T_6) at 1500 r/min and 3 N · m. (a) Phase a voltage and the three-phase currents. (b) Electromagnetic torque. Voltage scale: (50 V/div), current scale: (20 A/div), torque scale: (2 N · m/div), and time scale: (4 ms/div).

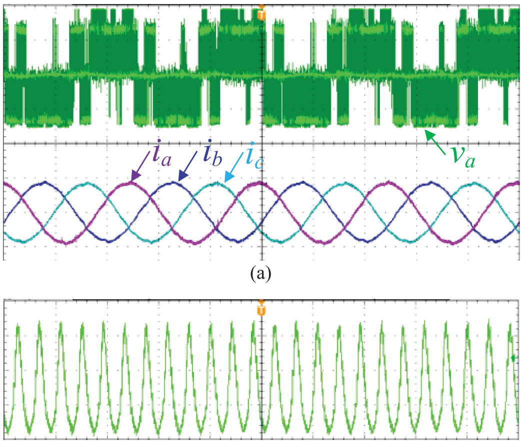

(a)

(b)

Fig. 24. Waveforms corresponding to the optimized point at 1500 r/min and 3 N · m. (a) Phase a voltage and the three-phase currents. (b) Electromagnetic torque. Voltage scale: (50 V/div), current scale: (20 A/div), torque scale: (2 N · m/div), and time scale: (4 ms/div).

C. MCSRM Performance at 1500 r/min With Distorted Phase Currents

The purpose of this section is to validate the optimization algorithm when the phase currents are distorted. Figs. 25–28 show the performance of the MCSRM at 1500 r/min and 3 N · m with a switching frequency of 5 kHz. Table V summarizes these experimental results. By comparing Tables IV and V, it can be noticed that the reference direct- and quadrature-axis currents, and the power factor at the same operating conditions are almost the same. But, the sixth-order harmonic of the torque (T_6), and the efficiency are different.

TABLE V
MCSRM PERFORMANCE AT 1500 r/min WITH A DISTORTED PHASE CURRENTS

Case	$[i_d, i_q]$(A)	I_m(A)	P_1(W)	Q_1(Var)	Displacement power factor		T_6(Nm)	η(%)
					Experimental	Calculated (9)		
Maximum torque per ampere (α=1)	[11.5, 11.5]	16.4	582	859	0.57	0.56	3	88
Maximum power factor (α=0)	[8.2, 16.6]	18.5	624	762	0.66	0.63	2.2	76
Minimum torque ripple	[7, 20]	21.2	675	862	0.64	0.62	1.9	65
Optimized point (α=0.4)	[9, 15.1]	17	598	763	0.64	0.62	2.3	83

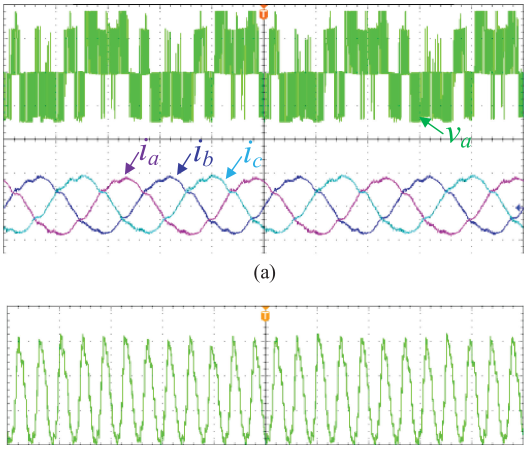

(a)

(b)

Fig. 25. Waveforms corresponding to the maximum torque per ampere at 1500 r/min and 3 N · m with distorted phase currents. (a) Phase a voltage and the three-phase currents. (b) Electromagnetic torque at 1500 r/min and 3 N · m. Voltage scale: (50 V/div), current scale: (20 A/div), torque scale: (2 N · m/div), and time scale: (4 ms/div).

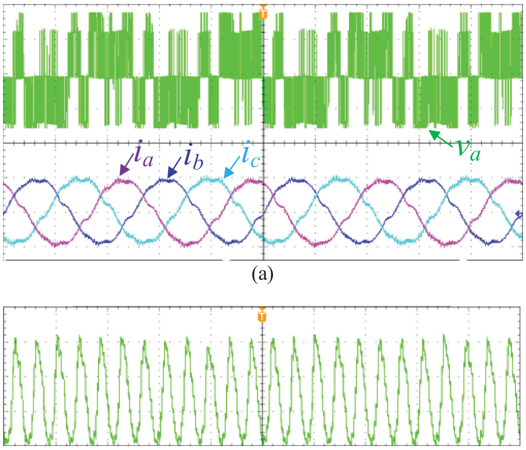

(a)

(b)

Fig. 26. Waveforms corresponding to the maximum power factor at 1500 r/min and 3 N · m with distorted phase currents. (a) Phase a voltage and the three-phase currents. (b) Electromagnetic torque at 1500 r/min and 3 N · m. Voltage scale: (50 V/div), current scale: (20 A/div), torque scale: (2 N · m/div), and time scale: (4 ms/div).

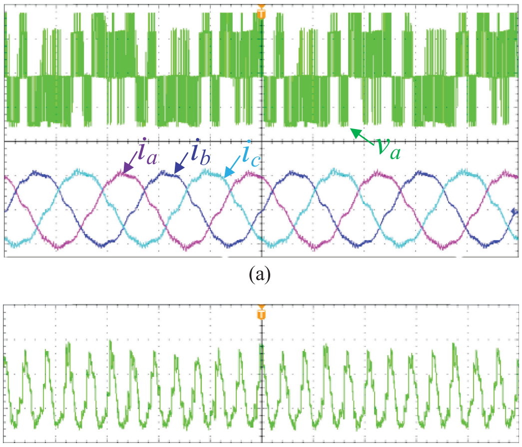

(a)

(b)

Fig. 27. Waveforms corresponding to the minimum torque ripple (T_6) at 1500 r/min and 3 N · m with distorted phase currents. (a) Phase a voltage and the three-phase currents. (b) Electromagnetic torque. Voltage scale: (50 V/div), current scale: (20 A/div), torque scale: (2 N · m/div), and time scale: (4 ms/div).

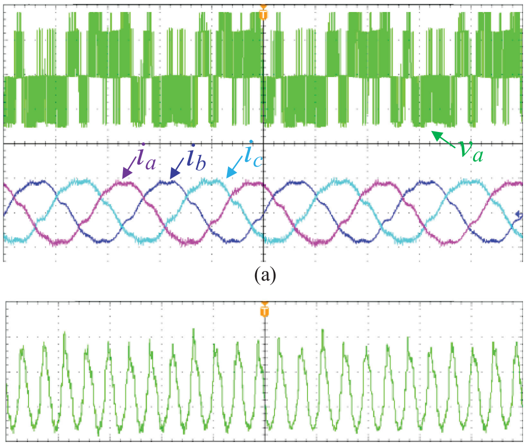

(a)

(b)

Fig. 28. Waveforms corresponding to the optimized point at 1500 r/min and 3 N · m with distorted phase currents. (a) Phase a voltage and the three-phase currents. (b) Electromagnetic torque. Voltage scale: (50 V/div), current scale: (20 A/div), torque scale: (2 N · m/div), and time scale: (4 ms/div).

The reference dq currents in Tables IV and V are the same as the average torque is a function of the fundamental direct- and quadrature-axis currents regardless of the distortion in the phase currents. Similarly, the power factor is due to the phase shift between the fundamental components of the phase voltage and phase current, and hence, the power factors in Tables IV and V are almost the same at the same operating conditions.

The calculation of efficiency in Tables IV and V is based on (21) as the ratio of the output mechanical power and the input electrical power. For nondistorted phase currents, the input electrical power is due to the fundamental components of the phase voltage and phase current. It can be calculated as the average value of the product of the phase current and phase voltage recorded in the experiments:

$$\begin{aligned} P &= \frac{3}{T_{\text{fund}}} \int_0^{T_{\text{fund}}} v_{\text{ph}}(t) i_{\text{ph}}(t) dt \\ &= 3 v_{\text{ph\_1}} v_{\text{ph\_1}} \cos(\theta_{v1} - \theta_{i1}) \end{aligned} \tag{22}$$

where T_{fund} is the period of the fundamental electrical cycle, and $v_{\text{ph}}(t)$ and $i_{\text{ph}}(t)$ are the instantaneous phase voltage and current profiles recorded in experiments, respectively. $v_{\text{ph\_1}}$ and $i_{\text{ph\_1}}$ are the rms values of the fundamental voltage and current components, respectively. θ_{v1} and θ_{i1} are the phase angles of the fundamental voltage and current components, respectively.

In the case of a distorted phase currents, there are current harmonics and voltage harmonics of the same harmonic order; thus, the real power components will exist for those harmonic orders, in addition to the fundamental components:

$$\begin{aligned} P &= \frac{3}{T_{\text{fund}}} \int_0^{T_{\text{fund}}} v_{\text{ph}}(t) i_{\text{ph}}(t) dt \\ &= \sum_{n=1}^{\infty} 3 v_{\text{ph\_}n} v_{\text{ph\_}n} \cos(\theta_{vn} - \theta_{in}) \end{aligned} \tag{23}$$

where $v_{\text{ph\_}n}$ and $i_{\text{ph\_}n}$ are the rms values of the nth harmonic order of the phase voltage and current components, respectively, and θ_{vn} and θ_{in} are their corresponding phase angles. The existence of the real power components of the harmonic orders results in a different electrical input power and, hence, different efficiency calculations compared to the case with a nondistorted phase currents. The contribution of the real power components of the harmonic orders can increase the total input electrical power such as the case in the minimum torque ripple operating point. In Table IV, 70% efficiency is achieved for the case of the minimum torque ripple with nondistorted phase currents. However, for the same operating condition, but with distorted currents, 65% efficiency is achieved, as shown in Table V.

The harmonic orders can also cause a reduction in the total input power and, hence, increase the efficiency of the motor compared to the case with the nondistorted phase currents. This can be observed when Tables IV and V are compared for the maximum torque per ampere operating point ($\alpha = 1$) and for the optimum operating point ($\alpha = 0.4$). Finally, Table V reveals that the efficiency of the motor at the maximum power factor operating point ($\alpha = 0$) does not change when the phase currents are distorted. It is worth mentioning that although the efficiency results are different when the phase currents are distorted, the relative characteristics of the four operating points in Tables IV and V are still the same. For instance, the maximum torque per ampere operating point still has the maximum efficiency, the maximum T_6, and the minimum power factor. Besides, the minimum torque ripple operating point has the minimum torque ripple and the minimum efficiency. Furthermore, the optimized operating point when $\alpha = 0.4$ merges the advantages of high power factor, high efficiency, and low T_6.

Notably, the current harmonics also create reactive power components. If these components are considered, the calculated power factor will be the true power factor instead of the displacement power factor. However, the real power and reactive power from the fundamental components are the largest among the other harmonics. Therefore, using the displacement power factor would be adequate for the optimization process.

VI. CONCLUSION

Torque ripple and power factor of MCSRMs with sinusoidal currents excitation are investigated in this article. Torque ripple in the MCSRM is mainly due to the sixth-order harmonic of the torque waveform. Hence, reducing the sixth-order harmonic can significantly reduce the torque ripple. Power factor reflects the saturation level of the MCSRM, and it depends on both the magnitude and angle of the current phasor. When the stator poles of phase a are aligned with the rotor poles, the maximum power factor is achieved when the current phasor is aligned with the stator poles of another phase, which generates torque in the positive rotation direction. The position of the current phasor at the aligned position is defined by the current excitation angle. Therefore, the maximum power factor is achieved when the current excitation angle is 60° for the three-phase 12/8 MCSRM. Simulation results show that the excitation angle corresponding to the maximum power factor deviates slightly from 60° due to the real power loss in phase resistance. An optimized control of MCSRM is presented, which aims to reduce the torque ripple and increase the power factor. Optimization results reveal that the operating point corresponding to the minimum torque ripple has the largest magnitude of phase current. Additionally, the operating point corresponding to the minimum phase current has the maximum torque ripple. The optimization results show that optimizing the power factor results in low torque ripple; therefore, the applied objective function includes the phase current and power factor only. The weighting coefficients of phase current and the power factor are selected so that the optimized operating point has lower phase current, lower torque ripple, and higher power factor. The proposed method is also validated by experimental results.

ACKNOWLEDGMENT

The authors would like to gratefully acknowledge Powersys Solutions for their support with JMAG software in the research presented herein. This article is dedicated to the memory of Iman Aghabali and Mehdi Eshaghian.

REFERENCES

[1] P. Azer, B. Bilgin, and A. Emadi, "Mutually coupled switched reluctance motor: Fundamentals, control, modeling, state of the art review and future trends," *IEEE Access*, vol. 7, pp. 100099–100112, 2019.

[2] A. D. Callegaro, B. Bilgin, and A. Emadi, "Radial force shaping for acoustic noise reduction in switched reluctance machines," *IEEE Trans. Power Electron.*, vol. 34, no. 10, pp. 9866–9878, Oct. 2019.

[3] P. Azer, J. Ye, and A. Emadi, "Advanced fault-tolerant control strategy for switched reluctance motor drives," in *Proc. IEEE Transp. Electrif. Conf. Expo*, Long Beach, CA, USA, 2018, pp. 20–25.

[4] P. Azer and J. Bauman, "An asymmetric three-level T-type converter for switched reluctance motor drives in hybrid electric vehicles," in *Proc. IEEE Transp. Electrif. Conf. Expo*, Detroit, MI, USA, 2019, pp. 1–6.

[5] P. L. Chapman and S. D. Sudhoff, "Design and precise realization of optimized current waveforms for an 8/6 switched reluctance drive," *IEEE Trans. Power Electron.*, vol. 17, no. 1, pp. 76–83, Jan. 2002.

[6] T. J. E. Miller, "Optimal design of switched reluctance motors," *IEEE Trans. Ind. Electron.*, vol. 49, no. 1, pp. 15–27, Feb. 2002.

[7] P. Azer, "Mutually coupled switched reluctance machines: Fundamentals, modeling, and control," Ph.D. dissertation, Dept. Elect. Comput. Eng., McMaster Univ., Hamilton, ON, Canada, Jun. 2020.

[8] G. J. Li, X. Y. Ma, G. W. Jewell, Z. Q. Zhu, and P. L. Xu, "Influence of conduction angles on single-layer switched reluctance machines," *IEEE Trans. Magn.*, vol. 52, no. 12, Dec. 2016, Art. no. 8108511.

[9] B. C. Mecrow, "Fully pitched-winding switched-reluctance and stepping-motor arrangements," *Proc. Inst. Elect. Eng. B—Electr. Power Appl.*, vol. 140, no. 1, pp. 61–70, Jan. 1993.

[10] T. Husain, W. Uddin, and Y. Sozer, "Performance comparison of short-pitched and fully pitched switched reluctance machines over wide speed operations," *IEEE Trans. Ind. Appl.*, vol. 54, no. 5, pp. 4278–4287, Sep./Oct. 2018.

[11] C. Ma, L. Qu, and Z. Tang, "Torque ripple reduction for mutually coupled switched reluctance motor by bipolar excitations," in *Proc. IEEE Int. Electr. Mach. Drives Conf.*, Chicago, IL, USA, May 2013, pp. 1211–1217.

[12] M. A. Kabir and I. Husain, "Hybrid excitation topologies for three-phase mutually coupled reluctance machine with standard inverters," in *Proc. IEEE Power Energy Soc. Gen. Meeting*, Denver, CO, USA, Jul. 2015, pp. 1–5.

[13] C. Ma and L. Qu, "Design considerations of switched reluctance motors with bipolar excitation for low torque ripple applications," in *Proc. IEEE Energy Convers. Congr. Expo*, Denver, CO, USA, Sep. 2013, pp. 926–933.

[14] M. A. Kabir and I. Husain, "Design of mutually coupled switched reluctance motors (MCSRMs) for extended speed applications using 3-phase standard inverters," *IEEE Trans. Energy Convers.*, vol. 31, no. 2, pp. 436–445, Jun. 2016.

[15] X. Y. Ma, G. J. Li, G. W. Jewell, Z. Q. Zhu, and H. L. Zhan, "Performance comparison of doubly salient reluctance machine topologies supplied by sinewave currents," *IEEE Trans. Ind. Electron.*, vol. 63, no. 7, pp. 4086–4096, Jul. 2016.

[16] X. Liang, G. Li, J. Ojeda, M. Gabsi, and Z. Ren, "Comparative study of classical and mutually coupled switched reluctance motors using multiphysics finite-element modeling," *IEEE Trans. Ind. Electron.*, vol. 61, no. 9, pp. 5066–5074, Sep. 2014.

[17] G. J. Li, Z. Q. Zhu, X. Y. Ma, and G. W. Jewell, "Comparative study of torque production in conventional and mutually coupled SRMs using frozen permeability," *IEEE Trans. Magn.*, vol. 52, no. 6, Jun. 2016, Art. no. 8103509.

[18] G. Li, J. Ojeda, S. Hlioui, E. Hoang, M. Lecrivain, and M. Gabsi, "Modification in rotor pole geometry of mutually coupled switched reluctance machine for torque ripple mitigating," *IEEE Trans. Magn.*, vol. 48, no. 6, pp. 2025–2034, Jun. 2012.

[19] B. Howey, B. Bilgin, and A. Emadi, "Design of a mutually coupled external-rotor direct drive e-bike switched reluctance motor," *IET Elect. Syst. Transp.*, vol. 10, no. 1, pp. 89–95, Mar. 2020.

[20] G. J. Li, K. Zhang, Z. Q. Zhu, and G. W. Jewell, "Comparative studies of torque performance improvement for different doubly salient synchronous reluctance machines by current harmonic injection," *IEEE Trans. Energy Convers.*, vol. 34, no. 2, pp. 1094–1104, Jun. 2019.

[21] R. Krishnan, "Dynamic modeling of permanent magnet synchronous machines," in, *Permanent Magnet Synchronous and Brushless DC Motor Drives*. Boca Raton, FL, USA: CRC Press, 2009.

[22] Y. Wang, D. Ionel, D. G. Dorrell, and S. Stretz, "Establishing the power factor limitations for synchronous reluctance machines," *IEEE Trans. Magn.*, vol. 51, no. 11, Nov. 2015, Art. no. 8111704.

[23] T. J. E. Miller, "Energy conversion and principles," in *Switched Reluctance Motors and Their Control*. Oxford, U.K.: Clarendon, 1993.

[24] B. Bilgin, J. W. Jiang, and A. Emadi, "Operational principles and modeling of switched reluctance machines," in *Switched Reluctance Motor Drives: Fundamentals to Applications*. Boca Raton, FL, USA: CRC Press, 2019.

[25] X. B. Liang, G. J. Li, J. Ojeda, M. Gabsi, and Z. Ren, "Comparative study of vibration and acoustic noise between classical and mutually coupled switched reluctance motors," in *Proc. IEEE Int. Conf. Elect. Mach.*, Marseille, France, Sep. 2012, pp. 2955–2960.

[26] C. Liu, F. Blaabjerg, W. Chen, and D. Xu, "Stator current harmonic control with resonant controller for doubly fed induction generator," *IEEE Trans. Power Electron.*, vol. 27, no. 7, pp. 3207–3220, Jul. 2012.

[27] P. Azer, S. Nalakath, and A. Emadi, "Model-based spatial harmonics vector compensation method for three-phase mutually coupled switched reluctance machine with sinusoidal current excitation," *IEEE Open J. Power Electron.*, vol. 1, pp. 216–226, 2020.

Peter Azer (Member, IEEE) received the B.S. and M.S. degrees from Ain Shams University, Cairo, Egypt, in 2013 and 2016, respectively, and the Ph.D. degree from McMaster University, Hamilton, ON, Canada, in 2020, all in electrical engineering.

He is currently a Postdoctoral Researcher with the McMaster Automotive Resource Center, Hamilton, where he is working on the design of power converters and the development of motor drives. His research interests include power electronics, motor drives, switched reluctance machines, multilevel inverters, fault-tolerant control, and system modeling.

Berker Bilgin (Senior Member, IEEE) received the Ph.D. degree in electrical engineering from the Illinois Institute of Technology, Chicago, IL, USA, in 2011, and the M.B.A. degree from the DeGroote School of Business, McMaster University, Hamilton, ON, Canada, in 2018.

He is currently an Assistant Professor with the Department of Electrical and Computer Engineering, McMaster University. He is also the Co-Founder and the Vice President of Engineering of Enedym, Inc., Hamilton, which is a spin-off company of McMaster University, Enedym, Inc., specializing in electric machines, electric motor drives (EMDs), advanced controls and software, and virtual engineering. He has authored and coauthored 104 journals and conference papers and three book chapters. He is the Principal Inventor/Co-Inventor of ten patents and pending patent applications. He is the Lead Editor and author of the textbook entitled *Switched Reluctance Motor Drives: Fundamentals to Applications* (Boca Raton, FL, USA: CRC Press, 2018). His current research interests include electric machines, switched reluctance motor drives, acoustic noise and vibration analysis and reduction, and power electronics and EMDs.

Dr. Bilgin was the Elected General Chair of the 2016 IEEE Transportation Electrification Conference and Expo. He is an Associate Editor for the IEEE TRANSACTIONS ON TRANSPORTATION ELECTRIFICATION.

Ali Emadi (Fellow, IEEE) received the B.S. and M.S. degrees (with highest distinction) from the Sharif University of Technology, Tehran, Iran, in 1995 and 1997, respectively, and the Ph.D. degree from Texas A&M University, College Station, TX, USA, in 2000, all in electrical engineering.

He is the Canada Excellence Research Chair Laureate with McMaster University, Hamilton, ON, Canada. He is also the holder of the NSERC/FCA Industrial Research Chair in Electrified Powertrains and Tier I Canada Research Chair in Transportation Electrification and Smart Mobility. Before joining McMaster University, he was the Harris Perlstein Endowed Chair Professor of Engineering and the Director of the Electric Power and Power Electronics Center and Grainger Laboratories, Illinois Institute of Technology, Chicago, IL, USA, where he established research and teaching facilities as well as courses in power electronics, motor drives, and vehicular power systems. He was the Founder, Chairman, and President of Hybrid Electric Vehicle Technologies, Inc.—a university spin-off company of the Illinois Institute of Technology. He is the President and Chief Executive Officer of Enedym, Inc., and Menlolab, Inc.,—two McMaster University spin-off companies. He is the Principal author/co-author of more than 500 journal and conference papers as well as several books, including *Vehicular Electric Power Systems: Land, Sea, Air, and Space Vehicles* (Boca Raton, FL, USA: CRC Press, 2003), *Energy Efficient Electric Motors* (Boca Raton, FL, USA: CRC Press, 2004), *Uninterruptible Power Supplies and Active Filters* (Boca Raton, FL, USA: CRC Press, 2005), *Modern Electric, Hybrid Electric, and Fuel Cell Vehicles: Fundamentals, Theory, and Design* (2nd ed. Boca Raton, FL, USA: CRC Press, 2009), and *Integrated Power Electronic Converters and Digital Control* (Boca Raton, FL, USA: CRC Press, 2009). He is also the Editor of the books entitled *Handbook of Automotive Power Electronics and Motor Drives* (Boca Raton, FL, USA: CRC Press, 2005) and *Advanced Electric Drive Vehicles* (Boca Raton, FL, USA: CRC Press, 2014). He is the co-editor of the *Switched Reluctance Motor Drives: Fundamentals to Applications* (Boca Raton, FL, USA: CRC Press, 2018).

Dr. Emadi was the Inaugural General Chair of the 2012 IEEE Transportation Electrification Conference and Expo and has chaired several IEEE and SAE conferences in the areas of vehicle power and propulsion. He was the founding Editor-in-Chief of the IEEE TRANSACTIONS ON TRANSPORTATION ELECTRIFICATION from 2014 to 2020.